RSC Advances

ROYAL SOCIETY OF CHEMISTRY

www.rsc.org/advances

Novel magnetically separable ZnO/AgBr/Fe_3O_4/Ag_3VO_4 nanocomposites with tandem n-n heterojunctions as highly efficient visible-light-driven photocatalysts

Maryam Shekofteh-Gohari, Aziz Habibi-Yangjeh*

Department of Chemistry, Faculty of Science, University of Mohaghegh Ardabili, P.O. Box 179, Ardabil, Iran.

Abstract

In the present work, novel magnetically separable ZnO/AgBr/Fe_3O_4/Ag_3VO_4 nanocomposites with different weight percents of Ag_3VO_4 were successfully prepared. The preparation method is a facile large–scale method with a low temperature of 96 °C. Characterization techniques of XRD, EDX, SEM, TEM, UV–vis DRS, FT-IR, PL, and VSM were applied to study microstructure, purity, morphology, spectroscopic, and magnetic properties of the resultant samples. Photocatalytic activity was evaluated by degradation of rhodamine B under visible-light irradiation. The results indicated that the nanocomposite with 10% of Ag_3VO_4 has the best activity. Photocatalytic activity of this nanocomposite is about 2.8 and 3.5-fold higher than those of the ZnO/AgBr/Fe_3O_4 and ZnO/Ag_3VO_4/Fe_3O_4 nanocomposites, respectively. The highly enhanced activity was attributed to formation of tandem n-n heterojunctions between ZnO, AgBr, and Ag_3VO_4 which suppresses recombination of the photogenerated electron-hole pairs. Furthermore, the enhanced activity of the nanocomposite for degradation of two more dye pollutants and a colorless pollutant was confirmed. Finally, the magnetic photocatalyst was recycled using external magnetic field with reasonable activity after four runs.

Keywords: ZnO/AgBr/Fe_3O_4/Ag_3VO_4; Magnetic photocatalyst; Visible-light-driven; Pollutants.

*Corresponding author: Aziz Habibi-Yangjeh, Tel: +98 045 33514702; Fax: +98 045 33514701; Email: ahabibi@uma.ac.ir

Introduction

It is believed that heterogeneous photocatalytic processes, as green and cost-effective technology, have potential to address different challenges in the field of environmental pollution, energy shortage, and global warming facing the human being in the present century.[1–3] In order to utilize the solar energy as source of the photocatalytic processes, it is essential that visible-light-driven photocatalysts with reasonable activity are provided. However, traditional photocatalysts such as TiO_2 and ZnO have wide band gaps. Consequently, they can mainly absorb UV fraction of the solar radiation, accounting for about 4% of the solar energy, which leads to their poor photocatalytic activities under visible-light irradiation.[4–6] Moreover, owing to their fast recombination of electron-hole pairs, they have low photocatalytic activity. Hence, preparation of highly enhanced visible-light-driven photocatalysts based on TiO_2 and ZnO has been the subject of many articles and at the present it is an interesting and attractive topic in the field of photocatalysis research.[7–20] In order to increase visible-light photocatalytic activity, two strategies can be used. The first one is enabling photocatalysts to absorb more energy from the solar irradiation and subsequently produce more photogenerated electron−hole pairs. The second one is preventing the photogenerated charge carriers from undesirable recombination, resulting in enhancement of electron−hole separation efficiency.[21–24] However, finding one-component photocatalyst with considerable activity under visible-light irradiation is almost impossible. Hence, we have to design multi-component photocatalysts with wide visible-light absorption range, low recombination of charge carriers, non-selective degradation ability for different pollutants, and reasonable stability. Recently, it was found that by combining two n-type semiconductors, n-n heterojunctions could be formed at the interface of them.[25–28] Due to formation of internal electric field at the interface of these semiconductors, separation of the

photogenerated electron-hole pairs could be greatly enhanced. Being as n-type semiconductors, by combining ZnO, AgBr, and Ag_3VO_4 with each other, n-n heterojunctions could be formed, resulting in enhanced photocatalytic activity.

On the other hand, after using photocatalysts in the reaction system, they cannot be entirely recycled, leading to generation of secondary pollution. Consequently, a major problem in large-scale utilization of photocatalysts is removal of them from the treated solutions. Magnetic photocatalysts, as new generation of photocatalysts, could tackle the above mentioned problem.[29] However, to the best of our knowledge, there is no report about the preparation and photocatalytic activity of the magnetic ZnO/AgBr/Fe_3O_4/Ag_3VO_4 nanocomposites with tandem n–n heterojunctions.

Based on the above considerations, we report novel magnetically separable ZnO/AgBr/Fe_3O_4/Ag_3VO_4 nanocomposites with different weight percents of Ag_3VO_4 prepared using a facile refluxing method at a low temperature of 96 °C. The microstructure, purity, morphology, spectroscopic, and magnetic properties of the prepared samples were studied using X-ray diffraction (XRD), energy dispersive analysis of X-rays (EDX), scanning electron microscopy (SEM), transmission electron microscopy (TEM), UV–vis diffuse reflectance spectroscopy (UV-vis DRS), Fourier transform-infrared spectroscopy (FT-IR), photoluminescence spectroscopy (PL), and vibrating sample magnetometry (VSM) techniques. Photocatalytic activity of the nanocomposites was investigated by degradations of rhodamine B (RhB), methylene blue (MB), methyl orange (MO), and phenol under visible-light irradiation. To further elucidate the photocatalytic degradation mechanism, a series of scavengers for the reactive species were employed. It was demonstrated that weight percent of Ag_3VO_4, refluxing time, and calcination temperature have considerable influence on the degradation reaction. Finally, the nanocomposite was magnetically separated from the treated solution after four successive cycles.

Experimental

Materials

Zinc nitrate ($Zn(NO_3)_2.4H_2O$), ferric chloride ($FeCl_3.6H_2O$), ferrous chloride ($FeCl_2.4H_2O$), silver nitrate, sodium bromide, ammonium-metavanadate, ammonia, and sodium hydroxide were purchased from Loba chemie. RhB, MO, MB, 2-propanol, ammonium oxalate, benzoquinone, and absolute ethanol were obtained from Merck and employed without further purification. Deionized water was used throughout this study.

Instruments

The XRD patterns were recorded by a Philips Xpert X-ray diffractometer with Cu Kα radiation (λ= 0.15406 nm), employing scanning rate of 0.04˚/sec in the 2θ range from 20˚ to 80˚. Surface morphology and distribution of particles were studied by LEO 1430VP SEM, using an accelerating voltage of 15 kV. The purity and elemental analysis of the products were obtained by EDX on the same SEM instrument. For SEM and EDX experiments, samples mounted on an aluminum support using a double adhesive tape coated with a thin layer of gold. The TEM investigations were performed by a Zeiss-EM10C instrument with an acceleration voltage of 80 kV. The DRS spectra were recorded by a Scinco 4100 apparatus. The FT-IR spectra were obtained by a Perkin Elmer Spectrum RX I apparatus. The PL spectra of the samples were studied using a Perkin Elmer (LS 55) fluorescence spectrophotometer with an excitation wavelength of 300 nm. The conditions were fixed in order to compare the PL intensities. UV-vis spectra for the degradation reaction were studied using a Cecile 9000 spectrophotometer. Magnetic properties of the samples were obtained using an alternating gradient force magnetometer (model AGFM, Iran). The ultrasound radiation was performed

using a Bandelin ultrasound processor HD 3100 (12 mm diameter Ti horn, 75 W, 20 kHz). The pH of solutions was measured using a Metrohm digital pH meter of model 691.

Preparation of the nanocomposites

Nanoparticles of Fe_3O_4 were prepared by chemical co-precipitation method that the detailed procedure was described elsewhere.[30] For preparation of the ZnO/AgBr/Fe_3O_4 nanocomposite, 0.128 g of Fe_3O_4 nanoparticles was dispersed into 150 mL of water by ultrasonic irradiation for 30 min in a cylindrical Pyrex reactor provided with water circulation arrangement to maintain its temperature at 25 °C. Then, 1.305 g of zinc nitrate and 0.236 g of silver nitrate were added to the formed dark brown suspension of Fe_3O_4 with mechanical stirring continued for 30 min. Afterwards, aqueous solution of sodium hydroxide (5 M) was slowly added to the solution under stirring until pH of the solution reached 10. Then, aqueous solution of potassium bromide (0.319 g dissolved in 20 mL of water) was dropwise added to the dark brown suspension under stirring. Afterwards, the formed orange suspension was stirred for 60 min and refluxed at about 96 °C for 60 min. The light brown product was centrifuged to get the precipitate and washed two times with water and ethanol and the product was magnetically separated. The precipitate was dried in an oven at 70 °C for 24 h.

In a typical procedure for preparation of the ZnO/AgBr/Fe_3O_4/Ag_3VO_4 (10%) nanocomposite, where %10 is the weight percent of Ag_3VO_4, 0.450 g of ZnO/AgBr/Fe_3O_4 nanocomposite was dispersed into 150 mL of water by ultrasonic irradiation for 10 min. Then, silver nitrate (0.058 g) was dissolved in the suspension and mechanically stirred for 60 min. After that, an aqueous solution of NaOH (5 M) was dropwise added into the solution under stirring at room temperature until the pH of the solution reached to 10. Then, an aqueous solution of ammonium metavanadate (0.013 g in 50 mL of water) was slowly added

to the formed suspension. Finally the suspension was refluxed at 96 °C for 60 min. The suspension was centrifuged to get the precipitate out and washed twice with water and ethanol and dried in an oven at 60 °C for 24 h. The schematic diagram for preparation of the nanocomposites can be illustrated in scheme 1.

[Please insert Scheme 1 about here]

Photocatalysis experiments

Photocatalysis experiments were performed in a cylindrical Pyrex reactor with about 400 mL capacity. Temperature of the reactor was maintained at 25 °C using a water circulation arrangement. The solution was mechanically stirred and continuously aerated by a pump to provide oxygen and complete mixing of the reaction solution. An LED source with 50 W was used as a visible-light source. The source was fitted on the top of the reactor. Prior to illumination, a suspension containing 0.1 g of the photocatalyst and 250 mL aqueous solution of RhB (1×10^{-5} M), MB (1.3×10^{-5} M), MO (1.05×10^{-5} M), or phenol (5.0×10^{-5} M), was continuously stirred in the dark for 60 min, to attain adsorption equilibrium. Samples were taken from the reactor at regular intervals and the photocatalyst removed before analysis by the spectrophotometer at 553, 664, 477, and 270 nm corresponding to the maximum absorption wavelengths of RhB, MB, MO, and phenol, respectively.

Results and discussion

Figure 1 exhibits XRD patterns of the Fe_3O_4, ZnO/Fe_3O_4, $ZnO/AgBr/Fe_3O_4$, $ZnO/Ag_3VO_4/Fe_3O_4$, and $ZnO/AgBr/Fe_3O_4/Ag_3VO_4$ nanocomposites with different weight percents of Ag_3VO_4. For pure Fe_3O_4, the diffraction peaks well match with the (220), (311), (400), (331), (422), (333), and (531) planes of the face-centered cubic structure (JCPDS file

number of 75-1610).[31] In the case of the ZnO/Fe_3O_4 nanocomposite, the diffraction peaks are ascribed to face-centered cubic Fe_3O_4 and wurtzite hexagonal crystalline ZnO (JCPDS file number of 65-3411).[32] For the $ZnO/AgBr/Fe_3O_4$ and $ZnO/Ag_3VO_4/Fe_3O_4$ nanocomposites, the diffraction patterns verify co-existence of all counterparts of the nanocomposites. Furthermore, in the $ZnO/AgBr/Fe_3O_4/Ag_3VO_4$ nanocomposites, diffraction peaks of Ag_3VO_4 are clearly observed that well matched with its monoclinic phase (JCPDS No. 43–0542).[33]

[Please insert Fig. 1 about here]

Purity of the samples was verified by EDX spectra and the results for the ZnO/Fe_3O_4, $ZnO/AgBr/Fe_3O_4$, $ZnO/Ag_3VO_4/Fe_3O_4$, and $ZnO/AgBr/Fe_3O_4/Ag_3VO_4$ (10%) samples are shown in Fig. 2a. It is evident that the samples have reasonable purity and all of the peaks are simply ascribed to elements of the resultant samples. Other peaks in these spectra are related to the elements applied for sputter coating of the samples on the EDX stage. Weight percents of Zn, O, Ag, Br, Fe, and V elements in the $ZnO/AgBr/Fe_3O_4/Ag_3VO_4$ (10%) nanocomposite are 37.5, 23.8, 17.0, 3.8, 11.4, and 6.4, respectively. Furthermore, EDX mapping was employed to display the element distributions in the $ZnO/AgBr/Fe_3O_4/Ag_3VO_4$ (10%) nanocomposite and the results are shown in Fig. 2b-h. It is evident that there is homogeneous distribution for the elements. Hence, it was concluded that the counterparts of the nanocomposite have uniformly combined to each other.

[Please insert Fig. 2 about here]

Morphology and junction between constituents of the $ZnO/AgBr/Fe_3O_4/Ag_3VO_4$ (10%) nanocomposite was investigated by SEM and TEM techniques and the results are shown in Fig. 3. For this nanocomposite, particles of Fe_3O_4, AgBr, and Ag_3VO_4 are clearly seen on ZnO sheets (Fig. 3a). Moreover, the TEM images of the nanocomposite confirm distribution

of Fe_3O_4, AgBr, and Ag_3VO_4 particles on the ZnO plates (Figs. 3b and 3c).

[Please insert Fig. 3 about here]

It is believed that photocatalytic activity is closely related to extent of generation, separation, and transfer of the photogenerated charge carriers.[34] UV-vis spectra of photocatalysts give useful information about extent of electron-hole pairs generated under the light irradiation. Hence, UV-vis DRS spectra of the resultant samples were provided and the results are shown in Fig. 4a. As can be seen, the ZnO/AgBr/Fe_3O_4, ZnO/Ag_3VO_4/Fe_3O_4, and ZnO/AgBr/Fe_3O_4/Ag_3VO_4 nanocomposites have intense absorption in the visible-light range. Consequently, under visible-light irradiation, more electron-hole pairs are generated on the nanocomposites, resulting in enhanced photocatalytic activity.

[Please insert Fig. 4 about here]

To characterize structural properties of the resultant samples, FT-IR spectra of the Fe_3O_4, ZnO/AgBr/Fe_3O_4, ZnO/Ag_3VO_4/Fe_3O_4, and ZnO/AgBr/Fe_3O_4/Ag_3VO_4 (10%) samples were provided and the spectra are shown in Fig. 4b. For the all samples, the broad absorption bands around 3200-3400 cm^{-1} are related to the O-H stretching vibration of adsorbed water. For the Fe_3O_4 nanoparticles, two characteristic peaks at 435 and 610 $cm^{-1}$are related to the vibrations of Fe–O bond.[29] For the samples with ZnO, the peak at 560 cm^{-1} is ascribed to the stretching vibration of the Zn-O bond.[28] In the case of the samples containing Ag_3VO_4, the peaks for Ag-V and V-O bonds were appeared about at 770, 880, and 920 cm^{-1}.[24] For the ZnO/AgBr/Fe_3O_4/Ag_3VO_4 (10%) nanocomposite, the peaks for Fe-O, Zn-O, Ag-V, and V-O bonds are clearly seen in the wavenumbers similar to its counterparts.

It is well known that magnetic properties of photocatalysts affect on magnetic separability of them. Hence, magnetization of the pure Fe_3O_4 nanoparticles and ZnO/AgBr/Fe_3O_4/Ag_3VO_4 (10%) nanocomposite were investigated and the results are shown in Fig. 5. As can be seen,

saturated magnetization for the Fe_3O_4 nanoparticles and the nanocomposite at 8500 Oe are 55.5 and 6.26 emu/g, respectively. Decrease of the magnetization of the nanocomposite is simply related to the presence of the nonmagnetic ZnO, AgBr, and Ag_3VO_4 particles along with the magnetic Fe_3O_4 nanoparticles. As can be seen in inset of Fig. 5, saturated magnetization of the nanocomposite is high enough to separate it from the solution after decontamination processes.

[Please insert Fig. 5 about here]

To investigate visible-light photocatalytic activity of the prepared samples, RhB, a widely used dye, was selected as a target pollutant. The degradation reaction was performed over the Fe_3O_4, ZnO/Fe_3O_4, $ZnO/AgBr/Fe_3O_4$, $ZnO/Ag_3VO_4/Fe_3O_4$, and $ZnO/AgBr/Fe_3O_4/Ag_3VO_4$ nanocomposites with different weight percents of Ag_3VO_4 and the results are displayed in Fig. 6a. Furthermore, photolysis of RhB under the visible-light irradiation (in absence of any photocatalyst) was carried out and the results are shown in this figure. It is evident that RhB has reasonable stability under the light irradiation for 360 min. It is observed that photocatalytic activity of the $ZnO/AgBr/Fe_3O_4/Ag_3VO_4$ nanocomposites with different weight percents of Ag_3VO_4 is higher than those of the Fe_3O_4, ZnO/Fe_3O_4, $ZnO/AgBr/Fe_3O_4$, and $ZnO/Ag_3VO_4/Fe_3O_4$ samples. Among the prepared samples, the $ZnO/AgBr/Fe_3O_4/Ag_3VO_4$ (10%) nanocomposite has the superior activity in the degradation reaction. After the light irradiation for 105 min, about 21, 16, 69, 65, and 98% of RhB were degraded over the Fe_3O_4, ZnO/Fe_3O_4, $ZnO/AgBr/Fe_3O_4$, $ZnO/Ag_3VO_4/Fe_3O_4$, and $ZnO/AgBr/Fe_3O_4/Ag_3VO_4$ (10%) samples, respectively. Figures 6b-e shows plots of absorbance *versus* wavelength for degradation of RhB over the ZnO/Fe_3O_4, $ZnO/AgBr/Fe_3O_4$, $ZnO/Ag_3VO_4/Fe_3O_4$, and $ZnO/AgBr/Fe_3O_4/Ag_3VO_4$ (10%) samples at various irradiation times. It is evident that intensity of the absorption peaks continuously decreases and there are not any blue-shifts for RhB absorption peaks centered at 554 nm.

Therefore, it was concluded that degradations of RhB over the nanocomposite takes place by aromatic ring-opening mechanism.[35,36]

[Please insert Fig. 6 about here]

In order to describe quantitatively photocatalytic activity of the resultant samples, observed first-order rate constants (k_{obs}) of the degradation reaction over the samples was calculated using the slope of equation $\ln[RhB] = \ln[RhB]_o - k_{obs}t$,[11] in which *[RhB]* and $[RhB]_o$ are concentrations of RhB in time of *t* and zero, respectively and the results are shown in Fig. 7a. As can be seen, the degradation rate constant increases with weight percent of Ag_3VO_4 up to 10 and then decreases. The degradation rate constants of RhB over the Fe_3O_4, ZnO/Fe_3O_4, $ZnO/AgBr/Fe_3O_4$, $ZnO/Ag_3VO_4/Fe_3O_4$, and $ZnO/AgBr/Fe_3O_4/Ag_3VO_4$ (10%) samples 4.92×10^{-4}, 4.74×10^{-4}, 102×10^{-4}, 82.6×10^{-4}, and 290×10^{-4} min^{-1}, respectively. Hence, activity of the nanocomposite is about 59, 61, 2.8, and 3.5-fold larger than those of the Fe_3O_4, ZnO/Fe_3O_4, $ZnO/AgBr/Fe_3O_4$, and $ZnO/Ag_3VO_4/Fe_3O_4$ samples, respectively. The emission intensity in a PL spectrum is closely related to recombination of photogenerated electron-hole pairs. Consequently, PL spectra have useful information about separation of photogenerated charge carriers. To disclose the enhanced activity of the $ZnO/AgBr/Fe_3O_4/Ag_3VO_4$ (10%) nanocomposite relative to the ZnO/Fe_3O_4, $ZnO/AgBr/Fe_3O_4$, $ZnO/Ag_3VO_4/Fe_3O_4$, $ZnO/AgBr/Fe_3O_4/Ag_3VO_4$(5%), and $ZnO/AgBr/Fe_3O_4/Ag_3VO_4$(20%) samples, their PL spectra were provided and the results are shown in Fig. 7b. As can be seen, compared with the other samples, intensity of the PL spectrum for the $ZnO/AgBr/Fe_3O_4/Ag_3VO_4$ (10%) nanocomposite shows significant decrease, suggesting efficiently separation of the charge carriers in this nanocomposite relative to the other samples. This result clearly indicates that hybridization of the ZnO/Fe_3O_4 with AgBr and Ag_3VO_4 particles promotes the separation of electron–hole pairs in the $ZnO/AgBr/Fe_3O_4/Ag_3VO_4$ nanocomposites. However, similar to

many multi-component photocatalysts[37-39], further increase in weight percent of Ag_3VO_4 leads to a decrease in the degradation rate constant. This may be due to agglomeration of the excess Ag_3VO_4 particles on the nanocomposites, which reduces the heterojunctions between Ag_3VO_4 and ZnO/AgBr/Fe_3O_4 counterparts, thereby separation of the charge carriers decreases. Hence, the amount of Ag_3VO_4 in the nanocomposites needs an optimum value.

[Please insert Fig. 7 about here]

To describe the enhanced activity of the nanocomposite, a hypothesized mechanism for separation of the charge carriers is presented (Fig. 8). The conduction band (CB) and valence band (CB) energies for ZnO, AgBr, and Ag_3VO_4 at the point of zero charge were calculated using Butler and Ginley model[40] and the results are shown in Table 1. Being as n-type semiconductors, the Fermi levels for ZnO, AgBr, and Ag_3VO_4 are close to their CB levels. The Fermi level of ZnO is more negative than those of AgBr and Ag_3VO_4. Hence, after contacting of ZnO with AgBr, electrons simply flow from ZnO to AgBr until their Fermi levels coincide.[41, 42] As a result, negative and positive charges are accumulated on AgBr and ZnO counterparts of the nanocomposite, respectively. Hence, an n-n heterojunction with the same Fermi level is formed (Fig. 8). Separation of the charge carriers by n-n heterojunction produces an internal electrostatic field directed from the ZnO to AgBr. Moreover, similar n-n heterojunction is formed after contacting ZnO with Ag_3VO_4. In this region, electrons transfer from ZnO to Ag_3VO_4. After reaching to equilibrium state, an electric field is formed at the interface area, directed from ZnO to Ag_3VO_4. As a result, two n-n heterojunctions are formed in the contacting region between ZnO with AgBr in one side and ZnO with Ag_3VO_4 in the other side. Hence, tandem n-n heterojunctions between these n-type semiconductors are formed.[28] Due to their narrow band gaps, under the visible-light irradiation, electron-hole pairs are generated on AgBr and Ag_3VO_4 counterparts of the ZnO/AgBr/Fe_3O_4/Ag_3VO_4 nanocomposites. The photogenerated electrons on the CB levels of AgBr and Ag_3VO_4 simply

transfer to the CB of ZnO with the help of the internal electrostatic field produced by tandem n-n heterojunctions. On the other hand, the VB energies of AgBr and Ag_3VO_4 are less positive than that of the ZnO. Consequently, the holes cannot transfer from the VB levels of AgBr and Ag_3VO_4 to that of the ZnO. Finally, after transfer of the electrons, holes and electrons are accumulated on the narrow band gap semiconductors and ZnO, respectively. As a result, due to formation of tandem n-n heterojunctions between ZnO with AgBr and ZnO with Ag_3VO_4, the charge carriers are spatially separated from each other, resulting in an increased lifetime for the electron-hole pairs. Afterwards, the separated charge carriers in the ZnO/AgBr/Fe_3O_4/Ag_3VO_4 nanocomposites effectively migrate to surface of the photocatalyst and participate in the degradation reactions, leading to enhanced activity relative to their counterparts. It is noteworthy that separation of the photogenerated charge carriers in AgBr and Ag_3VO_4 could not take place without formation of tandem n-n heterojunctions; because, the CB levels of AgBr and Ag_3VO_4 are less negative than the CB of ZnO. Hence, the photogenerated electrons cannot transfer from AgBr and Ag_3VO_4 to ZnO, resulting in more recombination of the photogenerated electron-hole pairs and high intensity of the PL spectrum. However, separation of the charge carriers in the nanocomposite was demonstrated by the PL spectra. Hence, formation of the tandem n-n heterojunctions between the three n-type semiconductors is confirmed.

[Please insert Fig. 8 about here]

In order to explore the role of reactive species responsible for degradation of RhB over the photocatalyst, the degradation reaction was conducted in the presence of a series of scavengers and the results are shown in Fig. 9. In the present work, benzoquinone, ammonium oxalate, and 2-PrOH were used as scavengers of $^{\bullet}O_2^-$, h^+, and $^{\bullet}OH$, respectively.[43] It is evident that decrease of the rate constant in the presence of scavengers is as benzoquinone > ammonium oxalate > 2-

PrOH. Hence, it is concluded that the effect of superoxide ions and holes on the degradation reaction is higher than that of hydroxyl radicals.

[Please insert Fig. 9 about here]

It is well known that preparation time of photocatalysts can considerably affect morphology, crystallinity, aggregation, and size of particles. Hence, the preparation time could remarkably affect photocatalytic activity. To find optimum preparation time, the ZnO/AgBr/Fe_3O_4/Ag_3VO_4 (10%) nanocomposite prepared by refluxing for 15, 30, 60, 120, and 240 minutes and the results are shown in Fig. 10a. It can be seen that the degradation rate constant increases with increasing the preparation time up to 60 min and then decreases. Decrease of the photocatalytic activity for the samples prepared with higher refluxing time could be related to more aggregation of the particles, resulting in decreased surface area of the photocatalyst.

[Please insert Fig. 10 about here]

To investigate the effect of calcination temperature on the photocatalytic activity, the ZnO/AgBr/Fe_3O_4/Ag_3VO_4 (10%) nanocomposite was calcined at 200, 300, 400, 500, and 600 °C for 2 h and the degradation reactions were carried out over them and the rate constant are shown in Fig. 10b. It can be seen that the degradation rate constant enhances with increasing calcination temperature up to 500 °C and then promptly decreases. To explore structure of the photocatalysts calcined at 500 and 600 °C, XRD patterns of the nanocomposite before and after calcinations are shown in Fig. 11a. As can be seen, after calcination of the nanocomposite at 500 °C, metallic silver is produced by decomposition of silver containing semiconductors in the nanocomposite.[44] The produced silver particles can increase transfer of electrons from the CB of Ag_3VO_4 and AgBr to that of the ZnO[45, 46], resulting in more separation of the charge carriers. However, activity of the nanocomposite calcined at 600 °C is very lower than those of the other samples. Morphologies of the nanocomposite calcined at

500 and 600 °C are compared in Figs. 11b and 11c. It is evident that there is a great changing in morphology of the nanocomposite after calcination at 600 °C. As can be seen, after calcination at 600 °C, plates of ZnO have tightly aggregated to each other and particles of other counterparts of the nanocomposite have considerably separated from the ZnO plates, resulting in decrease of the contact surface between counterparts of the nanocomposite. Hence, the photogenerated electron-hole pairs could not be separated efficiently from each other, leading to decrease the activity of the calcined photocatalyst at 600 °C.

[Please insert Fig. 11 about here]

Generally, wastewaters contain mixtures of different pollutants. Hence, it is essential that photocatalysts can degrade these pollutants non-selectively. To show ability of the nanocomposite calcined at 500 °C for degradation of different pollutants, degradations of RhB, MB, MO, and phenol over the nanocomposite was studied under the visible-light irradiation. Figure 12 shows plots of the degradation rate constants for RhB, MB, MO, and phenol over the calcined ZnO/Fe_3O_4, ZnO/AgBr/Fe_3O_4, ZnO/Ag_3VO_4/Fe_3O_4, and ZnO/AgBr/Fe_3O_4/Ag_3VO_4 (10%) samples. It is evident that photocatalytic activity of the ZnO/AgBr/Fe_3O_4/Ag_3VO_4 (10%) nanocomposite is much higher than those of the ZnO/Fe_3O_4, ZnO/AgBr/Fe_3O_4, ZnO/Ag_3VO_4/Fe_3O_4 samples. Hence, it is confirmed that the magnetic ZnO/AgBr/Fe_3O_4/Ag_3VO_4 nanocomposites has considerable activity in degradations of three different dye pollutants and one colorless pollutant.

[Please insert Fig. 12 about here]

For large-scale utilization of photocatalysts, besides photocatalytic activity, stability is another important factor from economical viewpoint. To investigate stability of the photocatalyst, the degradation experiments were carried out and the results are shown in Fig. 13. In each cycle, after using the nanocomposite, it was magnetically separated, washed with

ethanol and dried at 60 ºC for 24 h. It can be seen that the photocatalyst has reasonable stability during the degradation reaction and magnetic recycling from the treated solution. To investigate stability of the photocatalyst after fourth recycling, the XRD patterns of the nanocomposite before and after using for four cycles are shown in Fig. 13b. It is evident that very small amount of metallic silver is produced by photocorrosion of AgBr and Ag_3VO_4. Hence, it can be concluded that the magnetic nanocomposite has reasonable stability during the degradation processes.

[Please insert Fig. 13 about here]

Conclusions

Briefly, novel magnetically separable ZnO/AgBr/Fe_3O_4/Ag_3VO_4 nanocomposites, as highly efficient visible-light-driven photocatalysts, were successfully prepared by a facile large-scale procedure. Photocatalytic activity of the resultant samples was investigated by degradations of three dye pollutants and phenol under visible-light irradiation. Among the prepared samples, the ZnO/AgBr/Fe_3O_4/Ag_3VO_4 (10%) nanocomposite displayed the best activity. Activity of this nanocomposite was about 3.5 and 2.8-fold higher than those of the ZnO/Ag_3VO_4/Fe_3O_4 and ZnO/AgBr/Fe_3O_4 nanocomposites in degradation of RhB, respectively. The photocatalytic activity increases with increasing refluxing time up to 60 min and then decreases. Moreover, the results showed that the nanocomposite calcined at 500 °C has the best activity. Activity of the calcined nanocomposite in degradations of MB and MO is about 4 and 10-fold higher than that of the ZnO/AgBr/Fe_3O_4 nanocomposite, respectively. Hence, ability of the nanocomposite for efficiently degradation of different dye pollutants and phenol is confirmed. To describe the enhanced activity, a hypothesized mechanism for separation of the charge carriers was presented based on formation of tandem n-n heterojunctions between ZnO with AgBr and ZnO with Ag_3VO_4. Finally, it was confirmed

that the magnetic ZnO/AgBr/Fe_3O_4/Ag_3VO_4 nanocomposites has considerable activity after four successive runs.

Acknowledgements

The authors wish to acknowledge University of Mohaghegh Ardabili, for financial support of this work.

Notes and references

1 K. Li, X. An, K.H. Park, M. Khraisheh and J. Tang, *Catal. Today,* 2014, **224**, 3.

2 S. Dong, J. Feng, Y. Pi, L. Hu, X. Han, M. Liu, J. Sun and J. Sun, *RSC Advances*, 2015, **5**, 14610.

3 H. Ahmad, S.K. Kamarudin, L.J. Minggu and M. Kassim, *Renewable Sustainable Energy Rev.*, 2015, **43**, 599.

4 M. Pelaez, N.T. Nolan, S.C. Pillai, M.K. Seery, P. Falaras, A.G. Kontos, P.S.M. Dunlop, J.W.J. Hamilton, J.A. Byrne, K. O'Shea, M.H. Entezari and D.D. Dionysiou**,** *Appl. Catal. B: Environ.*, 2012, **125**, 331.

5 S.-M. Lam, J.-C. Sin, A.Z. Abdullah and A.R. Mohamed, *Desalin. Water Treatment*, 2012, **41**, 131.

6 M. Tahir and N.S. Amin, *Energy Conver. Manag.*, 2013, **76**, 194.

7 Y. Zang and R. Farnood, *Appl. Catal. B: Environ.*, 2008, **79**, 334.

8 K. Vignesh, A. Suganthi, M. Rajarajan and S.A. Sara, *Powder Technol.*, 2012, **224**, 331.

9 B. Krishnakumar, B. Subash and M. Swaminathan, *Separ. Purif. Technol.*, 2012, **85**, 35.

10 F. Xu, Y. Yuan, H. Han, D. Wu, Z. Gao and K. Jiang, *Cryst. Eng. Comm.*, 2012, **14**, 3615.

11 M. Pirhashemi and A. Habibi-Yangjeh, *Appl. Surf. Sci.*, 2013, **283**, 1080.

12 C. An, W. Jiang, J. Wang, S. Wang, Z. Ma and Y. Li, *Dalton Trans.*, 2013, **42** , 8796.

13 K. Dai, D. Li, L. Lu, Q. Liu, C. Liang, J. Lv and G. Zhu, *Appl. Surf. Sci.*, 2014, **314**, 864.

14 C. Dong, K.-L.Wu, M.-R. Li, L. Liu and X.-W. Wei, *Catal. Commun.*, 2014, **46**, 32.

15 F. Chang, J. Zhang, Y. Xie, J. Chen, C. Li, J. Wang, J. Luo, B. Deng and X. Hu, *Appl. Surf. Sci.*, 2014, **311** , 574.

16 J. Yi, L. Huang, H. Wang, H. Yu and F. Peng, *J. Hazard. Mater.*, 2015, **284**, 207.

17 J. Ma, K. Wang, L. Li, T. Zhang, Y. Kong and S. Komarneni, *Ceram. Int.*, 2015, **41**, 2050.

18 S. Shaker-Agjekandy and A. Habibi-Yangjeh, *Mater. Sci. Semiconductor Process.*, 2015, **34**, 74.

19 S. Yi, X. Yue, D. Xu, Z. Liu, F. Zhao, D. Wang and Y. Lin, *New J. Chem.*, 2015, **39**, 2917.

20 C. Liu, C. Cao, X. Luo and S. Luo, *J. Hazard. Mater.*, 2015, **285**, 319.

21 Y. Wang, Q. Wang, X. Zhan, F. Wang, M. Safdar and J. He, *Nanoscale*, 2013, **5**, 8326.

22 C.-C. Shen, Q. Zhu, Z.-W. Zhao, T. Wen, X. Wang and A.-W. Xu, *J. Mater. Chem. A*, 2015, **3**, 14661.

23 W.-S. Wang, H. Du, R.-X. Wang, T. Wen and A.-W. Xu, *Nanoscale*, 2013, **5**, 3315.

24 Q. Zhu, W.-S. Wang, L. Lin, G.-Q. Gao, H.-L. Guo, H. Du and A.-W. Xu, *J. Phys. Chem. C*, 2013, **117**, 5894.

25 Y. Yan, H. Guan, S. Liu and R. Jiang, *Ceram. Int.*, 2014, **40**, 9095.

26 M. Xu, T. Ye, F. Dai, J. Yang, J. Shen, Q. He, W. Chen, N. Liang, J. Zai and X. Qian, *Chem. Sus. Chem.*, 2015, **8**, 1218.

27 F. Kiantazh and A. Habibi-Yangjeh, *Mater. Sci. Semiconductor Process.*, 2015, **39**, 671.

28 M. Pirhashemi and A. Habibi-Yangjeh, *Ceram. Int.*, 2015, **41**, 14383.

29 S.-Q. Liu, Environ. *Chem. Lett.*, 2012, **10**, 209.

30 R. Massart, *Magnetics IEEE Trans.*, 1981, **17**, 1247.

31 J. Safari and Z. Zarnegar, *J. Mol. Struct.*,2014, **1072**, 53.

32 B.G. Mishra and G.R. Rao, *J. Mol. Catal. A: Chem.*, 2006, **243**, 204.

33 C.-M. Huang, G.-T. Pan, Y.-C.M. Li, M.-H. Li and T.C.-K. Yang, *Appl. Catal. A: General*, 2009, **358**, 164.

34 H.H. Mohamed and D.W. Bahnemann, *Appl. Catal. B: Environ.*, 2012, **128**, 91.

35 X. Li and J. Ye, *J. Phys. Chem. C*, 2007, **111**, 13109.

36 A. Martinez-dela Cruz and U.M. Garcia Perez, *Mater. Res. Bull.*, 2010, **45**, 135.

37 C. Xing, Z. Wu, D. Jiang and M. Chen, *J. Colloid Interf. Sci.*, 2014, **433**, 9.

38 S.-W. Cao, X.-F. Liu, Y.-P. Yuan, Z.-Y. Zhang, Y.-S. Liao, J. Fang, S.C.J. Loo, T.C. Sum and C. Xue, *Appl. Catal. B: Environ.*, 2014, **147**, 940.

39 L. Zhang, X. Wang, Q. Nong, H. Lin, B. Teng, Y. Zhang, L. Zhao, T. Wu and Y. He, *Appl. Surf. Sci.*, 2015, **329**, 143.

40 S.R. Morrison, Electrochemistry at semiconductor and oxidized metal electrode, Plenum, New York, 1980.

41 C. Shifu, Z. Wei, L. Wei, Z. Huaye, Y. Xiaoling and C. Yinghao, *J. Hazard. Mater.*, 2009, **172**, 1415.

42 W. Wang, J. Wang, Z. Wang, X. Wei, L. Liu, Q. Ren, W. Gao, Y. Liang and H. Shi, *Dalton Trans.*, 2014, **43**, 6735.

43 Z. He, Y. Shi, C. Gao, L. Wen, J. Chen and S. Song, *J. Phys. Chem. C*, 2015, **118**, 389.

44 M. Shekofteh-Gohari and A. Habibi-Yangjeh, *Solid State Sci.*, 2015, **48**, 177.

45 C. Liu, C. Cao, X. Luo and S. Luo, *J. Hazard. Mater.*, 2015, **285**, 319.

46 W. Cao, L. Chen and Z. Qi, *J. Mol. Catal. A: Chem.*, 2015, **401**, 81.

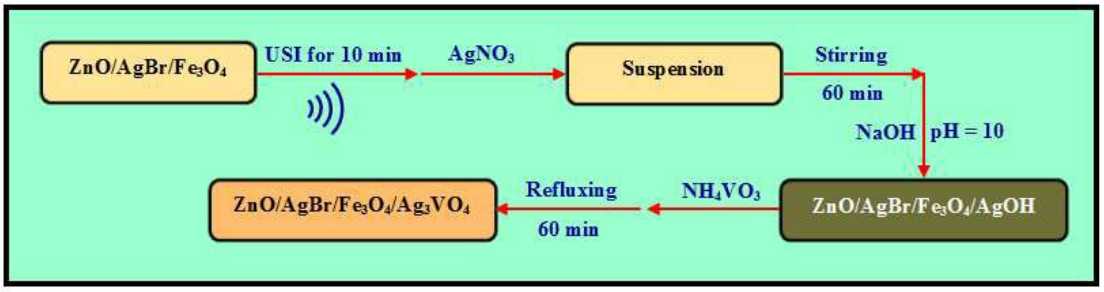

Scheme 1. The schematic diagram for preparation of the $ZnO/AgBr/Fe_3O_4/Ag_3VO_4$ nanocomposites.

Caption for the figures:

Fig. 1 XRD patterns for the Fe_3O_4, ZnO/Fe_3O_4, $ZnO/AgBr/Fe_3O_4$, $ZnO/Ag_3VO_4/Fe_3O_4$, and $ZnO/AgBr/Fe_3O_4/Ag_3VO_4$ nanocomposites with different weight percents of Ag_3VO_4.

Fig. 2 (a) EDX spectra for the ZnO/Fe_3O_4, $ZnO/AgBr/Fe_3O_4$, $ZnO/Ag_3VO_4/Fe_3O_4$, and $ZnO/AgBr/Fe_3O_4/Ag_3VO_4$ (10%) samples. (b)-(h) EDX mapping of the $ZnO/AgBr/Fe_3O_4/Ag_3VO_4$ (10%) nanocomposite.

Fig. 3 (a) SEM image of the $ZnO/AgBr/Fe_3O_4/Ag_3VO_4$ (10%) nanocomposite. (b) and (c) TEM images of the $ZnO/AgBr/Fe_3O_4/Ag_3VO_4$ (10%) nanocomposite with two magnifications.

Fig. 4 (a) UV-vis DRS spectra for the $ZnO/AgBr/Fe_3O_4$, $ZnO/Ag_3VO_4/Fe_3O_4$, and $ZnO/AgBr/Fe_3O_4/Ag_3VO_4$ nanocomposites with different weight percents of Ag_3VO_4. (b) FT-IR spectra for the Fe_3O_4, $ZnO/AgBr/Fe_3O_4$, $ZnO/Ag_3VO_4/Fe_3O_4$, and $ZnO/AgBr/Fe_3O_4/Ag_3VO_4$ (10%) samples.

Fig. 5 Magnetization curves for the Fe_3O_4 nanoparticles and $ZnO/AgBr/Fe_3O_4/Ag_3VO_4$ (10%) nanocomposite.

Fig. 6 (a) Photodegradation of RhB over the Fe_3O_4, ZnO/Fe_3O_4, $ZnO/AgBr/Fe_3O_4$, $ZnO/Ag_3VO_4/Fe_3O_4$, and $ZnO/AgBr/Fe_3O_4/Ag_3VO_4$ nanocomposites with different weight percents of Ag_3VO_4. UV–Vis spectra for degradation of RhB under visible-light irradiation over the (b) ZnO/Fe_3O_4, (c) $ZnO/AgBr/Fe_3O_4$, (d) $ZnO/Ag_3VO_4/Fe_3O_4$, and (e) $ZnO/AgBr/Fe_3O_4/Ag_3VO_4$ (10%) nanocomposite.

Fig. 7 (a) The degradation rate constants of RhB over different samples. (b) PL spectra for the ZnO/Fe_3O_4, $ZnO/Ag_3VO_4/Fe_3O_4$, $ZnO/AgBr/Fe_3O_4$, $ZnO/AgBr/Fe_3O_4/Ag_3VO_4$ (5%), $ZnO/AgBr/Fe_3O_4/Ag_3VO_4$ (10%), and $ZnO/AgBr/Fe_3O_4/Ag_3VO_4$ (20%) nanocomposites.

Fig. 8 Hypothesized mechanism for separation of the charge carriers in the $ZnO/AgBr/Fe_3O_4/Ag_3VO_4$ nanocomposites via tandem n-n heterojunctions.

Fig. 9 The degradation rate constant of RhB over the $ZnO/AgBr/Fe_3O_4/Ag_3VO_4$ (10%) nanocomposite in presence of various scavengers.

Fig. 10 (a) The degradation rate constants of RhB over the $ZnO/AgBr/Fe_3O_4/Ag_3VO_4$ (10%) nanocomposite prepared at different refluxing times. (b) The degradation rate constants of RhB over the $ZnO/AgBr/Fe_3O_4/Ag_3VO_4$ (10%) nanocomposite calcined at different temperatures.

Fig. 11 (a) XRD patterns for the $ZnO/AgBr/Fe_3O_4/Ag_3VO_4$ (10%) nanocomposite before and after calcinations at 500 and 600 °C. (b) SEM images of the $ZnO/AgBr/Fe_3O_4/Ag_3VO_4$ (10%) nanocomposite calcined at 500 and 600 °C.

Fig. 12 The degradation rate constants of RhB, MB, MO, and phenol over the ZnO/Fe_3O_4, $ZnO/AgBr/Fe_3O_4$, $ZnO/Ag_3VO_4/Fe_3O_4$, and $ZnO/AgBr/Fe_3O_4/Ag_3VO_4$ (10%) nanocomposites calcined at 500 °C.

Fig. 13 (a) Reusability of the ZnO/AgBr/Fe_3O_4/Ag_3VO_4 (10%) nanocomposite for four successive runs. (b) The XRD patterns of the nanocomposite before and after fourth recovery.

Figure 1

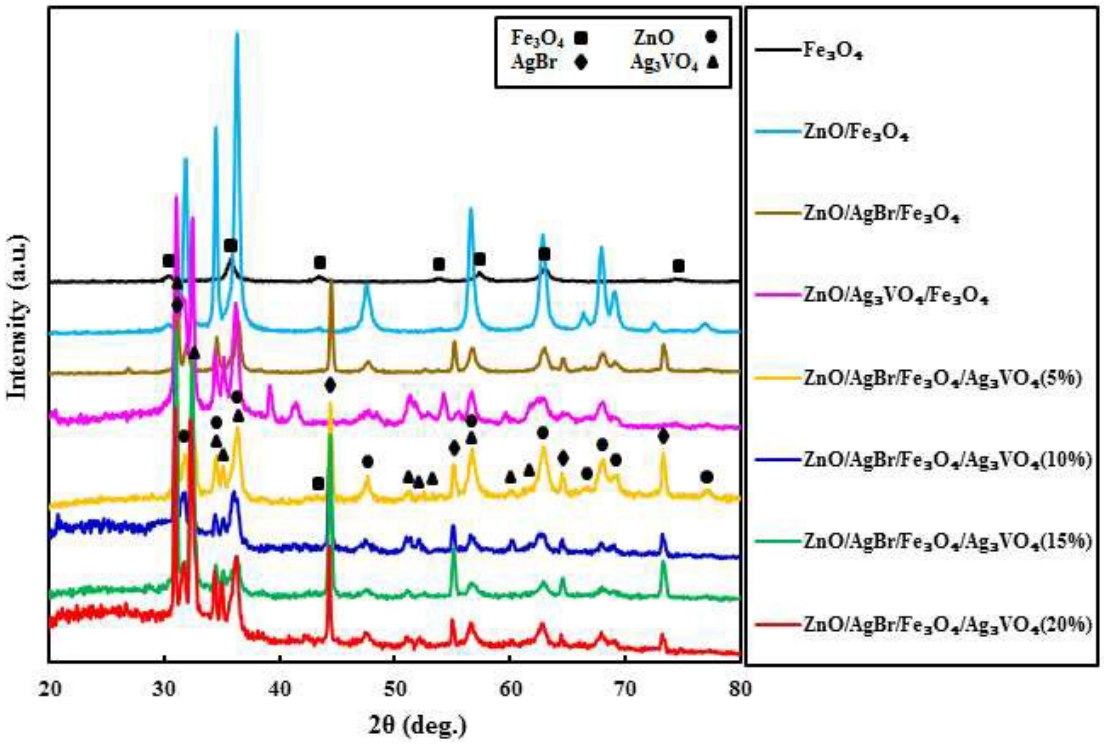

Figure 2

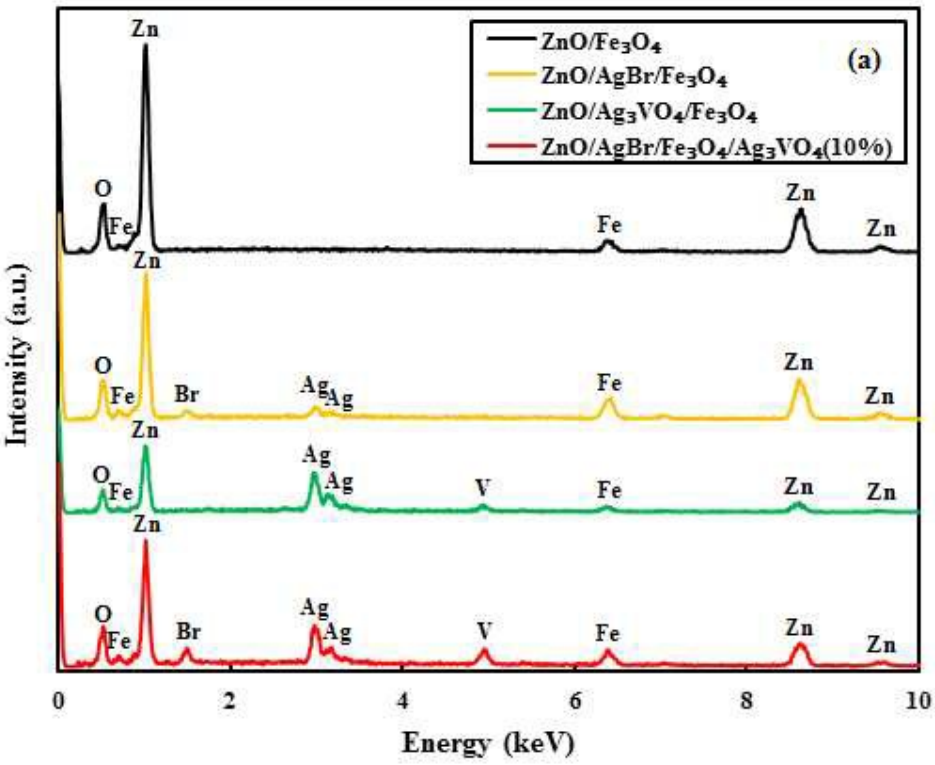

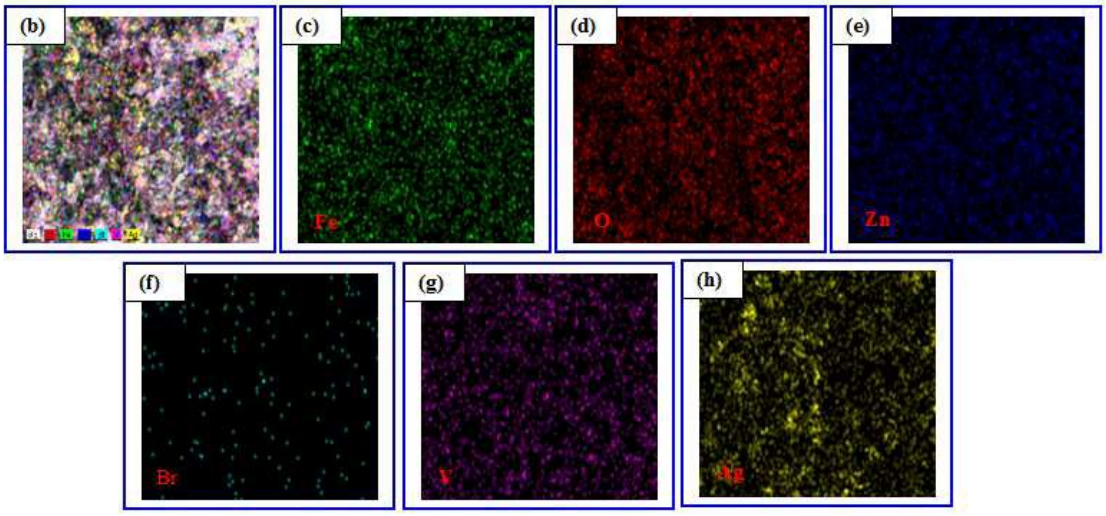

Figure 3

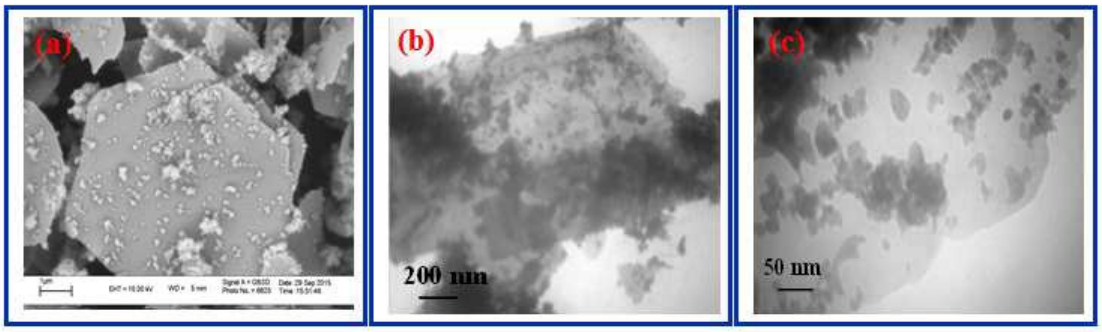

Figure 4

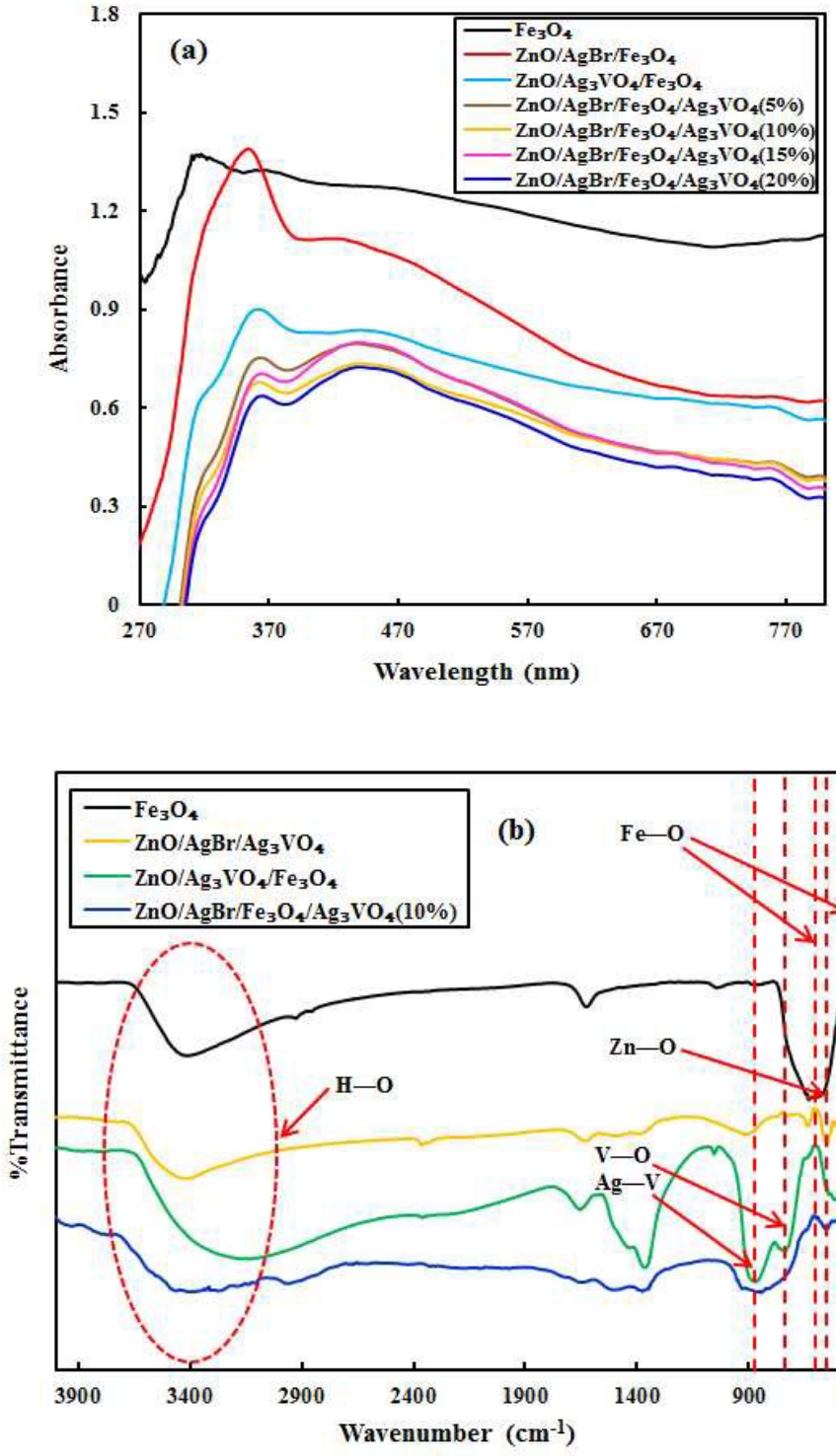

Figure 5

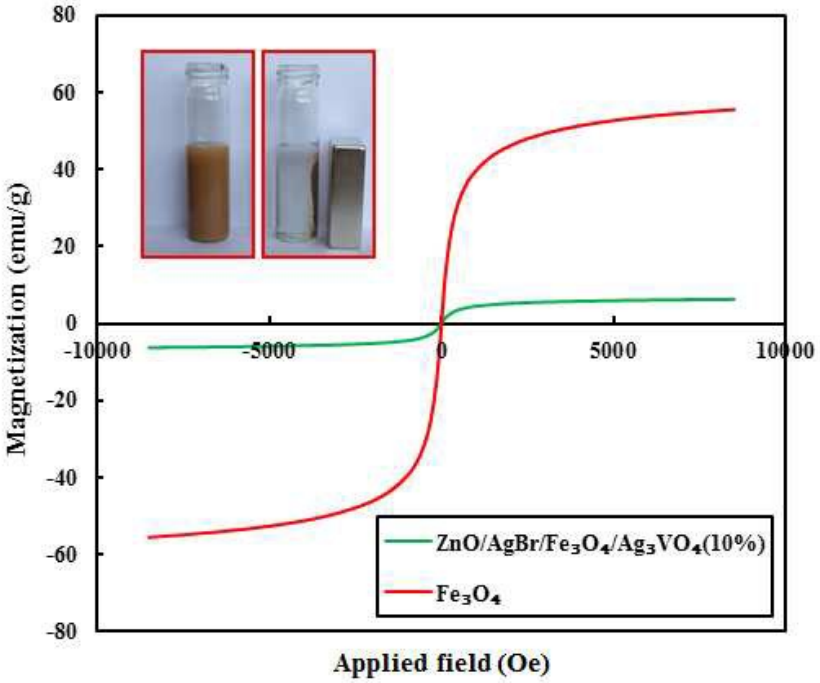

Figure 6

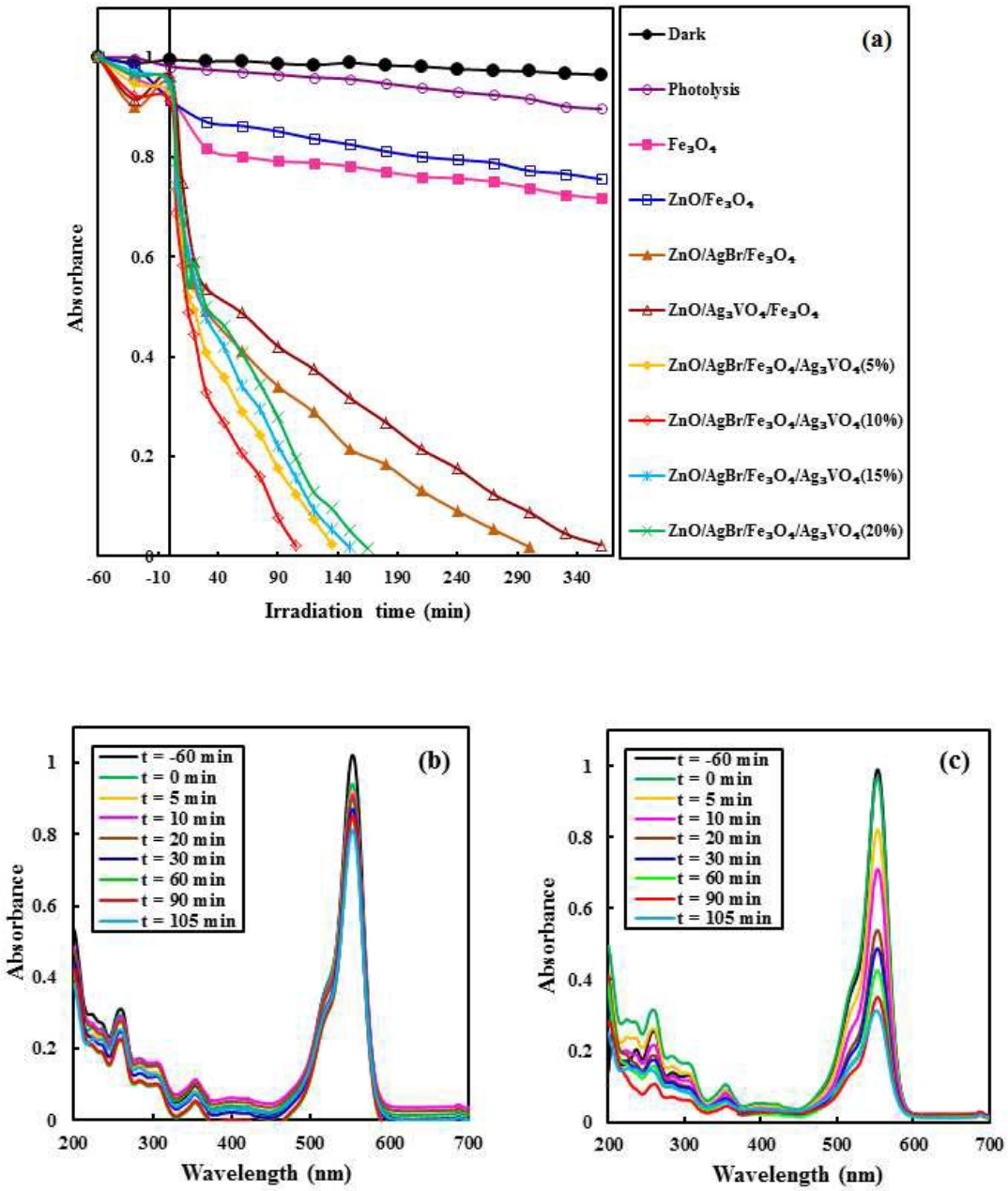

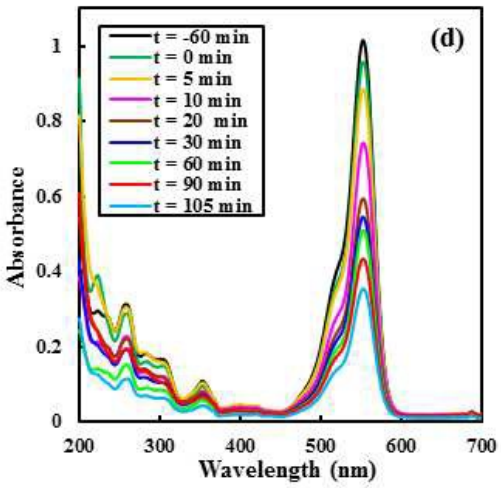

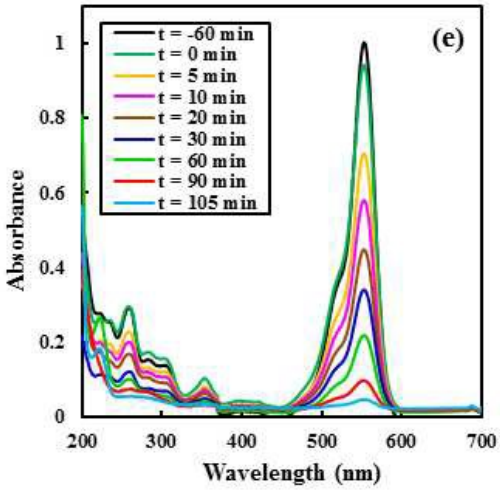

Figure 7

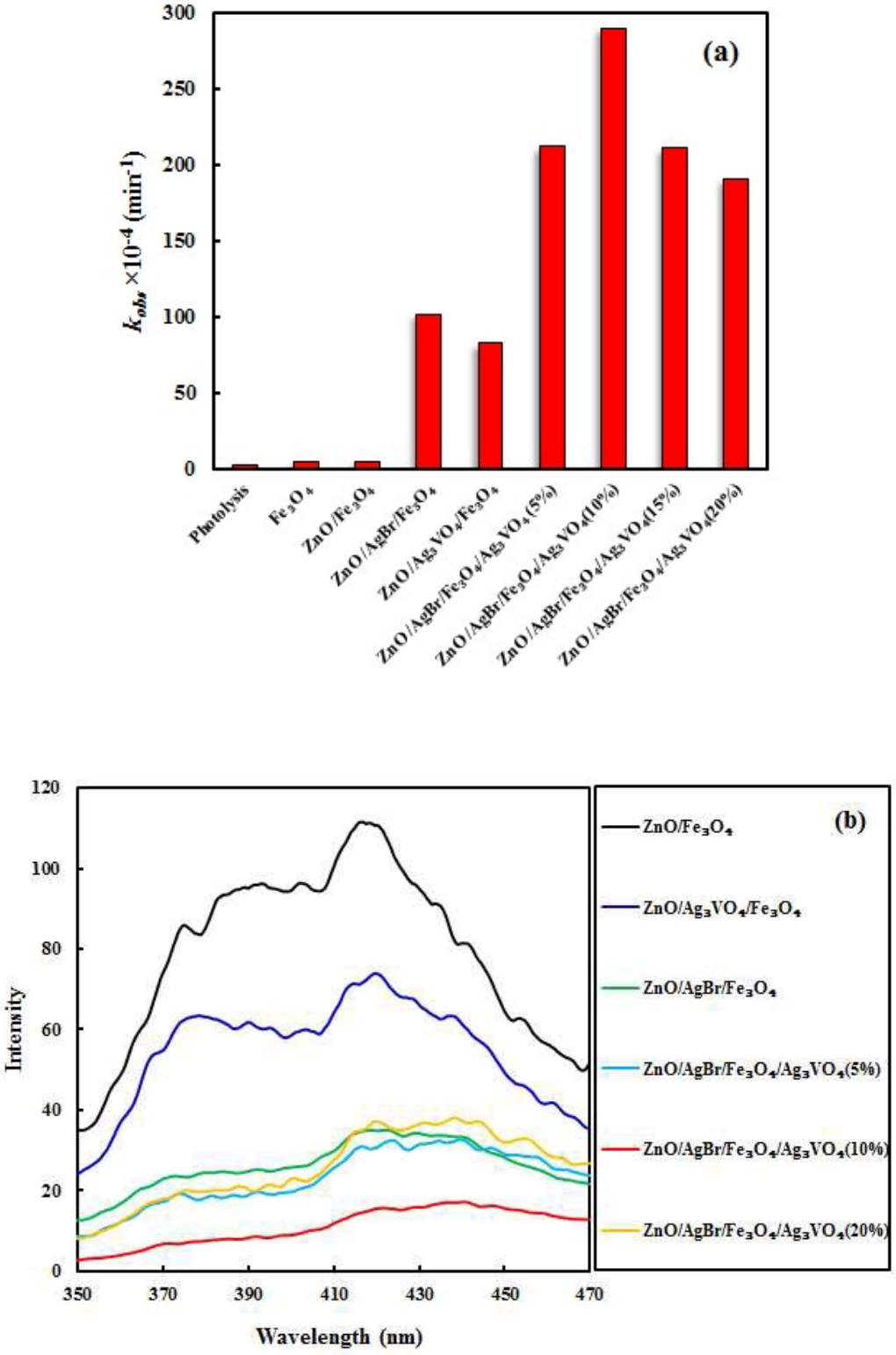

Figure 8

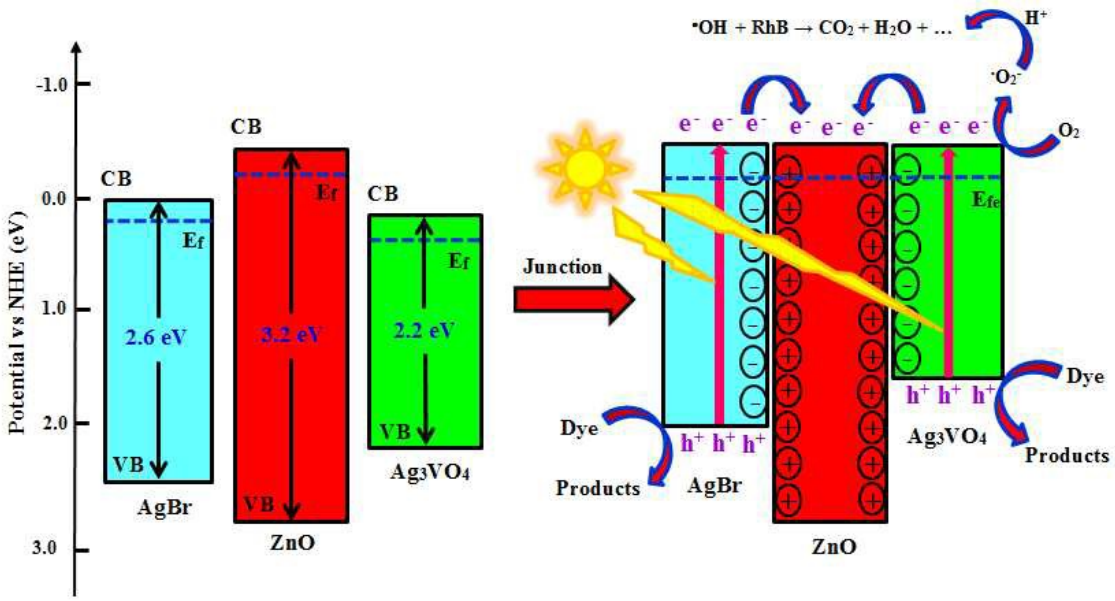

Figure 9

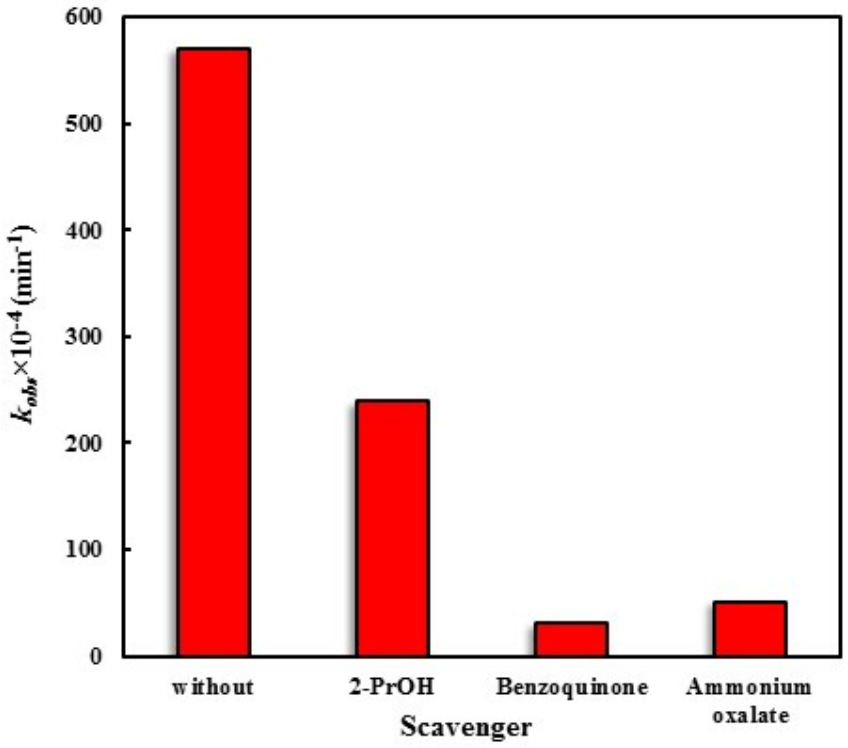

Figure 10

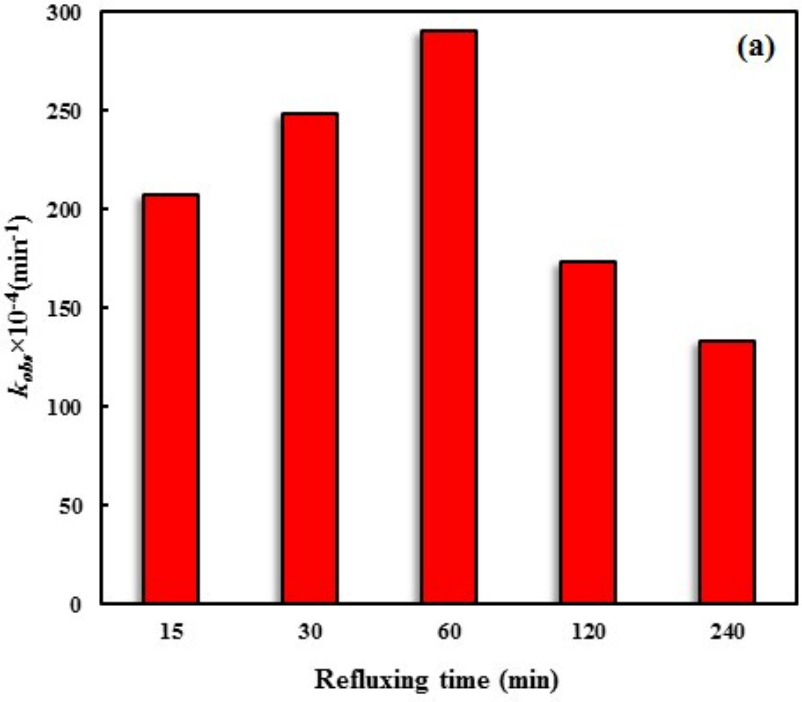

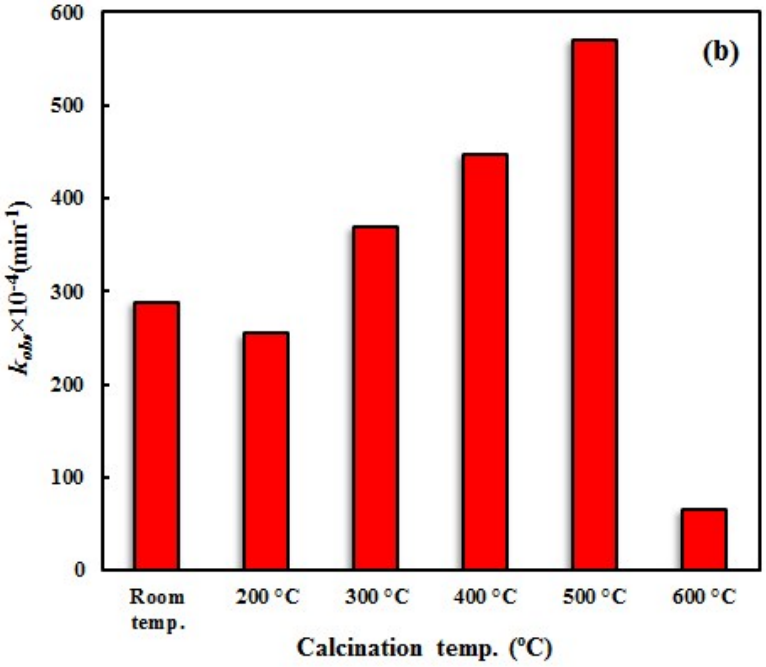

Figure 11

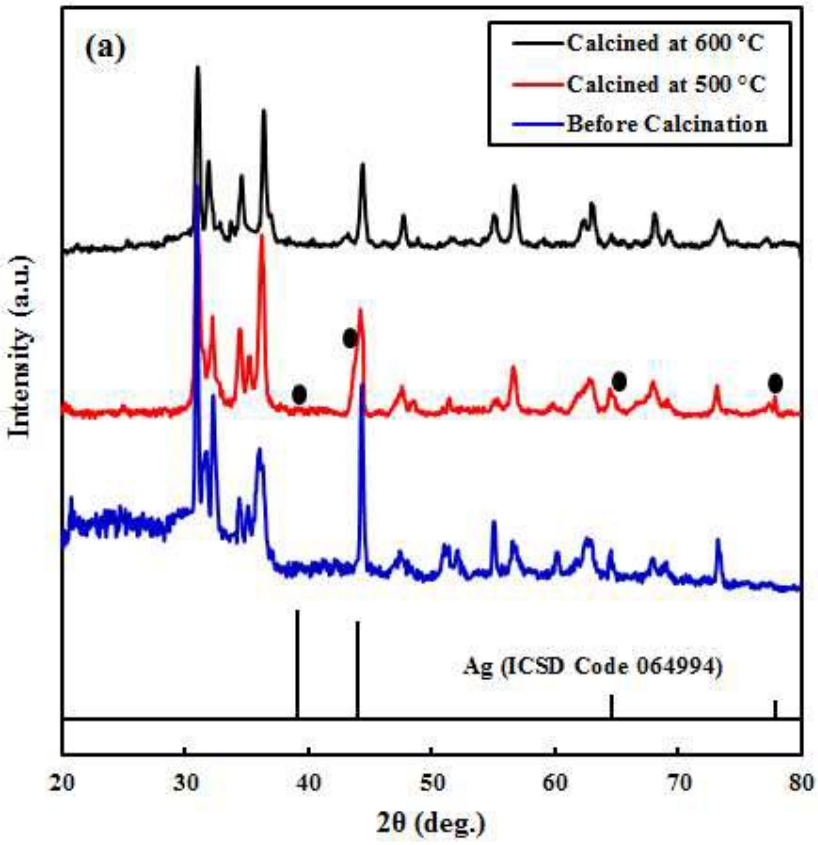

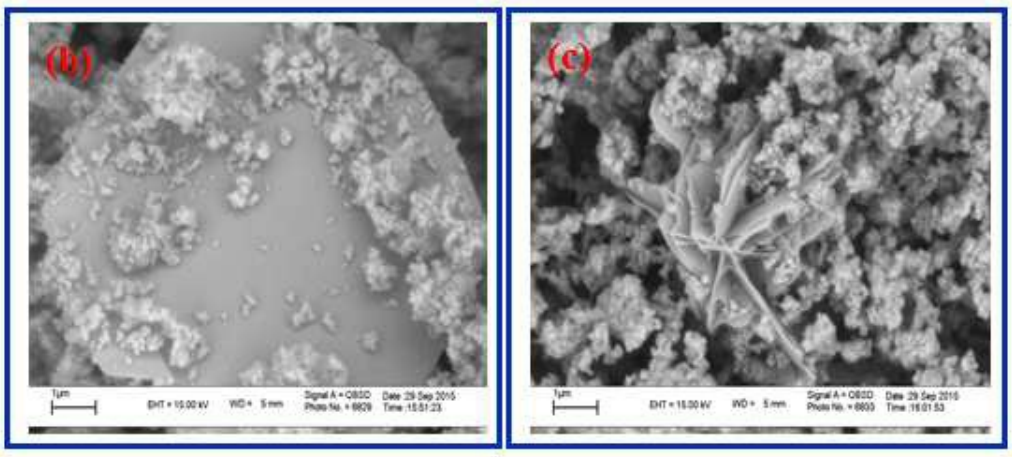

Figure 12

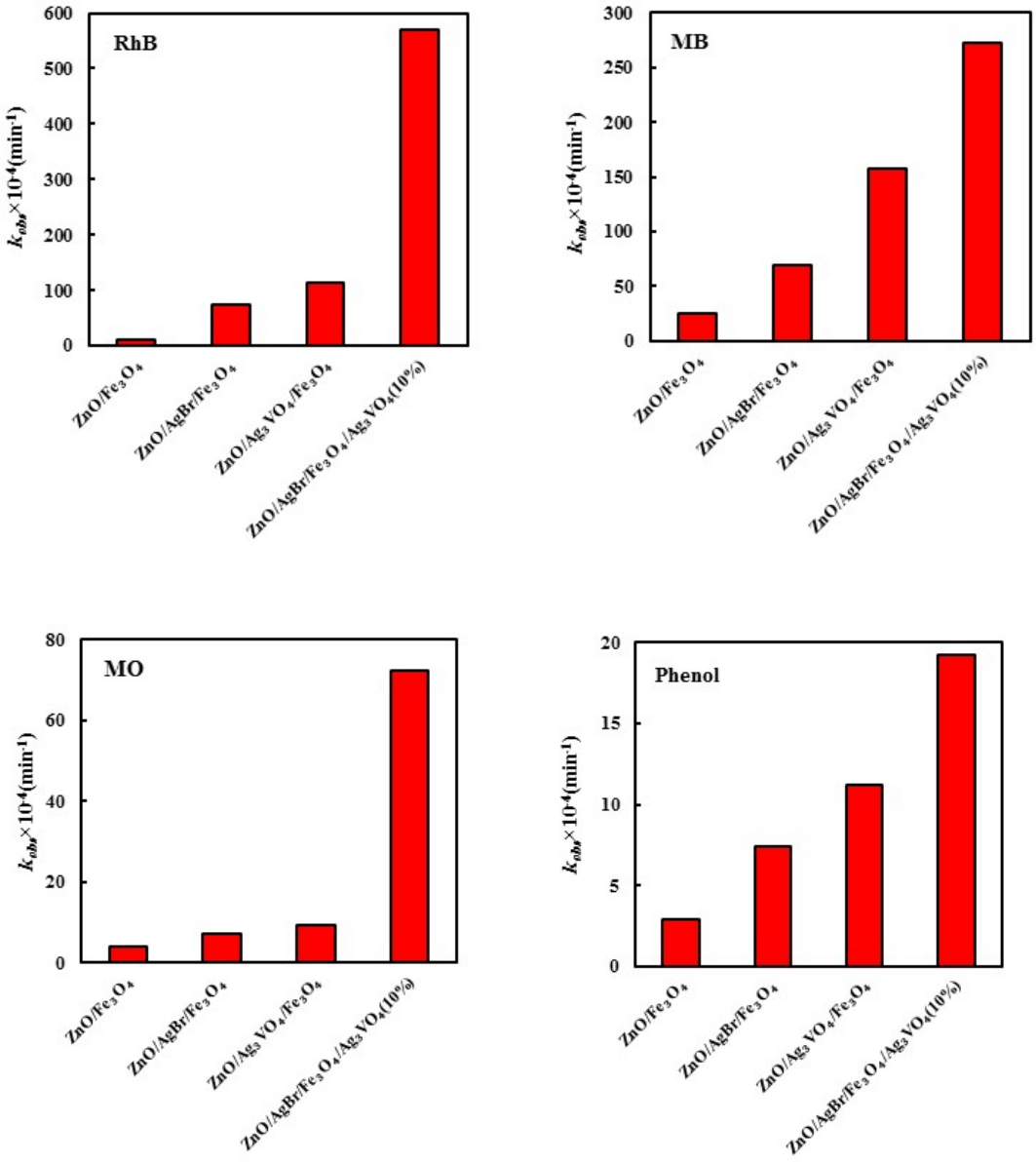

Figure 13

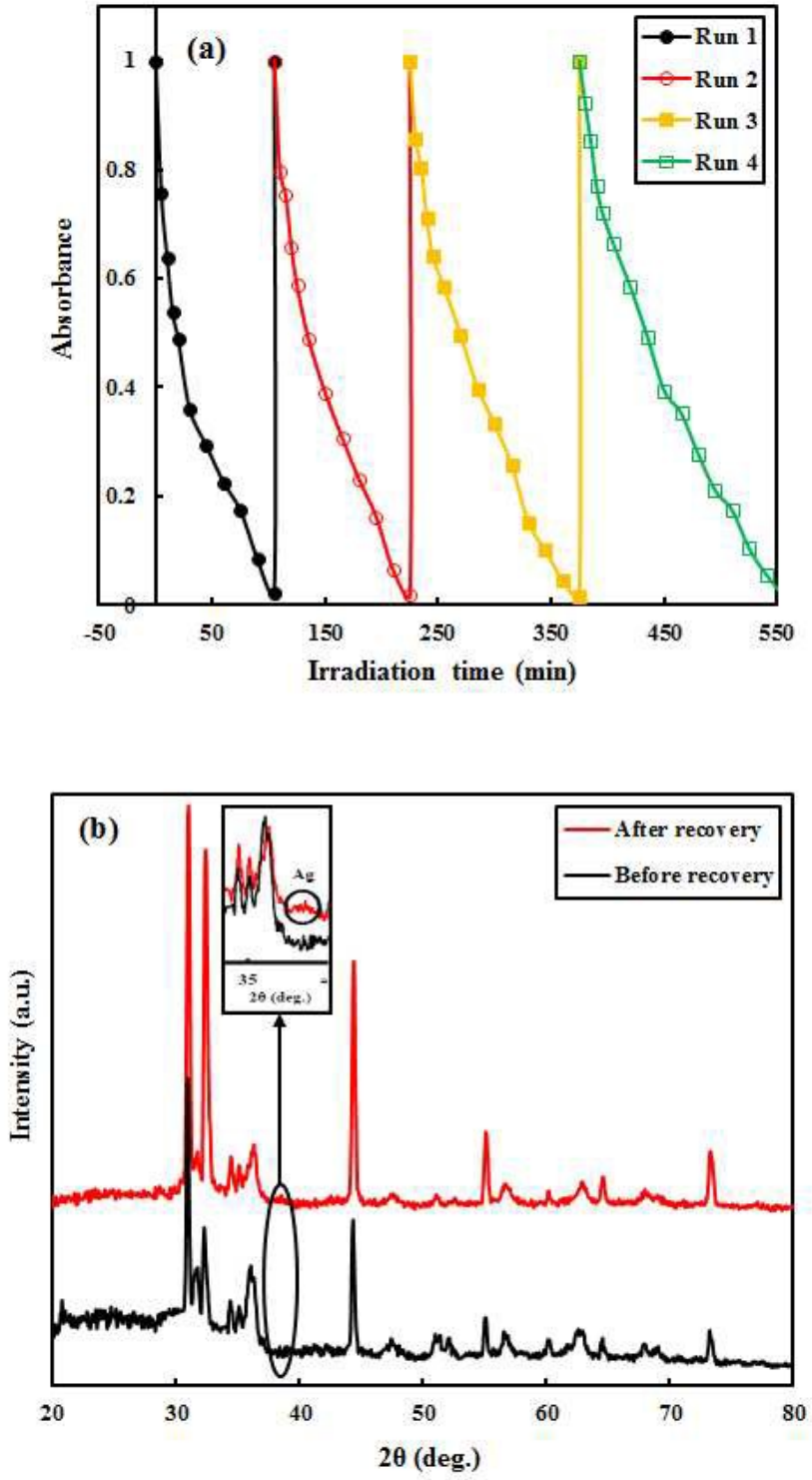

Graphical abstract: